Strojniški vestnik - Journal of Mechanical Engineering 70(2024)5-6, 211-222
DOI:10.5545/sv-jme.2024.966
Original Scientific Paper
Received for review: 2024-02-29
Received revised form: 2024-03-08
Accepted for publication: 2024-03-26

On Experimental Determination of Poisson's Ratio for Rock-like Materials using Digital Image Correlation

Pino Koc*
University of Ljubljana, Faculty of Mathematics and Physics, Slovenia

This article compares the two most used strain determination experimental techniques, the strain gauges and the digital image correlation (DIC), which are used here to determine the static Poisson's ratio of rock-like materials under a compressive loading. While the strain gauge technique measures the strains on the small patch of the underlying material on the spot, where the strain gauge is applied, DIC is a novel optical full-field technique that can measure the strains over the entire region of interest of the specimen. The key research question presented in this paper and research significance is to what extent the measurement of Poisson's ratio is improved by leveraging the richness of the full-field measurements compared to the conventional strain gauge technique. To this purpose, the hypothesis was tested through virtual experiments in which a numerical simulation of a uniaxial compression test with a cylindrical, rock-like sample was created to mimic the strain gauge and DIC measurement techniques, as well as by conducting an actual compression test on a sandstone material. In contrast to conventional strain gauges, novel optical techniques such as stereo DIC proved to be able to capture the macroscopic Poisson coefficient with higher precision, thus reducing the margin of error.
Keywords: Poisson's ratio, digital image correlation, strain gauge, rock-like materials, uniaxial compression test

Highlights
- *The concept of virtual experimentation is used to compare strain gauge and DIC techniques to evaluate the standard deviation of the reconstructed population of Poisson's ratio.*
- *To measure the Poisson's ratio and compare both techniques, a uniaxial compression test was performed on a cylindrical sandstone sample.*
- *In contrast to conventional strain gauges, novel optical techniques such as stereo DIC proved to be able to measure the macroscopic Poisson's ratio with a higher precision.*
- *Since the determination is influenced by signal-to-noise ratio, a simple engineering criterion for calculation is proposed.*

0 INTRODUCTION

The rock mass is a diverse geological material typically characterized by numerous intrinsic defects such as cracks, joints, bedding planes, and faults embedded in aggregates of crystals and amorphous particles bound by varying amounts of cementing materials [1] and [2]. These intrinsic inhomogeneities contribute to a heterogeneous microstructural response at the microscale, often resulting in complex material behaviour [3]. To accurately model the macroscopic response of such rock structures, a homogenization principle using a representative volume element (RVE) [4] and [5] is commonly applied [6] and [7] to predict the effective material behaviour at the macroscale [8] and [9]. Such models are based on bonded particle modelling techniques that have been proposed to account for different mechanical responses and behaviours of geomaterials [10]. For example, Zhou et al. [11] and [12] comprehensively investigated the importance of modelling the internal microstructure and interaction effects through bonded particle model–μ-discrete fracture network (BPM–μDFN) modelling to analyse the size effect and associated strength variability for rock considering the microstructure and strain rate.

Typically, in such models a set of material parameters must be determined from an experimental response of corresponding mechanical test [13]. For this purpose, contact and noncontact techniques can be used to measure the mechanical response, and specifically, with an advent development of optical technologies, new possibilities for material characterization have been opened. The use of 3D scanners and cameras enabled a precise measurement of displacements and strains of the tested sample, enabling engineers to assess material behaviour [14] and [15] and to make informed design decisions [16].

The digital image correlation (DIC) [17] is one of the most commonly used optical techniques for strain measurement. In DIC, the sequentially captured images are processed to extract valuable information for observation of both local and global behaviour of structures. In addition, DIC can operate in real time and provides the ability to monitor structural responses under dynamic loading conditions. This feature makes DIC a powerful tool for various applications ranging from material testing [18] and [19] and characterisation [20] and [21], to structural analysis [22] and product

*Corr. Author's Address: University of Ljubljana, Faculty of Mathematics and Physics, Jadranska 19, 1000 Ljubljana, Slovenia, pino.koc@fmf.uni-lj.si

development [23]. A concise literature survey listing studies of DIC applications to geotechnical materials, using different materials, test types, specimen shapes and loading conditions is given in the work of Tang et al. [24].

Using of DIC has unlocked the potential for the development of novel material characterization strategies like virtual fields method (VFM) [25] and finite element model updating (FEMU) [26] to [29], where the richness of measured displacements and strains over the entire region of interest (ROI) can be analysed to accurately capture material behaviour. As an example, Zhang et al. [30] developed a novel DIC-based methodology for crack identification in a jointed rock mass. Their DIC results obtained on synthetic sandstone specimens demonstrate that the cracking process is successfully identified by the displacement vectors and strain localization. Similarly, Chai et al. [31] used DIC for damage characterisation of rock-like specimens under uniaxial compression, where they showed that the failure mechanism of the sample is shear failure followed by tensile failure. In a recent study, Chen et al. [32] investigated the influence of the arrangement of flaw geometry on the interaction of flaw configurations and failure characteristics of sandstone specimens. Utilising the potential of full-field DIC measurements, the crack configuration was found to have a significant influence on the failure characteristics of the rock, and three typical crack coalescence modes were found. The results and experiments provide a better understanding of the interaction between flaws and the failure characteristics of the rock under compressive and shear loading.

The full potential of full-field strain measurement using DIC was clearly demonstrated by Luo et al. [33]. They investigated the deformation mechanisms of stratified rock-like material when different interlayer thickness ratios and length-to-width ratios of the specimens were selected. Similarly, Wang et al. [34] utilised the potential of DIC and acoustic emission techniques to monitor the evolution of the heterogeneous strain field and development of microcracks in specimens in a real time. They concluded that the strain localisation zones developed mainly near the holes and joints, that both the shape of the holes and the inclination of the joints had a significant influence on the collapse mode of specimens, and that the inclination of the joints played a dominant role of mechanical responses of the double-hole specimens.

While the above studies were conducted for static test configurations, Xing et al. [35] utilised DIC for dynamic testing of cylindrical rock specimens using the Hopkinson pressure bar system. In their study, they observed the propagation of compression waves within the sandstone specimen at different strain rates from quasi-static to 120 s^{-1} and measured the corresponding stress-strain curves using conventional strain gauges and the DIC technique.

A particularly interesting result of their analysis is that strain gauges show an increase in Young's modulus with increasing strain rate and ductile properties after the peak stress, which is different from a static measurement. Interestingly, the curves obtained with DIC give different results. The modulus is unchanged at all strain rates, and the higher the strain rate, the higher the strain at peak stress. Obviously, improper strain measurement can lead to erroneous results and incorrect characterisation. A similar conclusion was reached by Zhang and Zhao [36], who found that the measurement of specimen strains using the signals from strain gauges on the bars is not very accurate because the strain to failure is very small for brittle and quasi-brittle materials.

While strain gauges are widely used for metallic materials, their use for rock-like materials is somewhat limited. Hsieh et al. [37] measured both axial and circumferential strains of cylindrical specimens using diametrically positioned strain gauges. However, Liu et al. [38] point out that the measurement error of this method is large because the adhesion of the strain gauges increases the local stiffness of the specimens. The application of this method is cumbersome, and the strain gauges are disposable. In their work, they developed a new test method for measuring circumferential strains, but the test has its limitations as it does not provide information about the strain field in the entire area. In addition, Isah et al. [39] presented that the strain gauges do not capture the strains after the post-peak regime, which is mainly due to the damage of the strain gauges by cracks in the rock. As presented in their study, strain gauges are also inclined to measure the local response of the underlying material structure and represent the response at the mesoscale. Sun et al. [40] have recently discussed this aspect and analysed the influence of position and number of strain gauges on the characterisation of attenuation and moduli of rocks with mesoscopic heterogeneities.

The main focus and research significance of this study is to analyse to what extent the measurement of Poisson's ratio is improved by DIC full-field measurements compared to the strain gauge technique. To this end, the margin of error in the measurement of the static Poisson's ratio is evaluated for both

measurement methods when applied to a virtual and a real experiment with rock-like material. For the virtual experiment, the linear-elastic two-phase material with hard rock inclusions is modelled for the compression test of a cylindrical sample. It is shown that with DIC the richness of the measured strain field can be exploited, resulting in a lower margin of error [41], whereas conventional strain gauges tend to measure the local response of the material beneath the gauge. Therefore, a large number of measurements need to be repeated to obtain accurate values. This is particularly problematic with specimens for which only a few test opportunities are available. Comparison of both methods gives us insight into advantages of full-field DIC measurements and potential drawbacks when using strain gauges.

In this article the experimental work is divided into two parts. The first part, given in article's Section 1, introduces the concept of virtual experimentation. Within this concept, (i) the FEM is used to model the response of the cylindrical compression specimen; then, calculated surface strains are exported from FEM model for further manipulation (ii) to mimic the virtual strain gauge measurement, and (iii) to mimic a complete DIC measurement chain from image deformation to the calculation of surface strains. Once the strains are reconstructed by both virtual strain gauges and DIC, the measurements are repeated for hundreds of different positions of the strain gauges on the same deformed sample. Similarly, the DIC measurement was repeated for hundreds of different ROI positions. Using the measured strains, a population of Poisson's ratios is calculated, and the margin of error is evaluated for both the strain gauge and the DIC technique.

This method is used to analyse the extent to which the strain gauge measurement is influenced by the heterogeneity of the material structure, as the measurement is taken over a limited area over which the strain gauge is bonded. On the other hand, DIC allows the data are captured not only for a single small area, but for the entire surface of the sample. These data are used to determine the mean value of the Poisson's ratio with a higher precision than with the conventional strain gauge technique.

In the second experimental part, Section 2 of this article, the same procedure is repeated for a real experiment using a cylindrical sandstone sample. However, it should be emphasised that performing a real strain gauge measurement for hundreds or dozens of repetitions is cumbersome. Therefore, the concept of virtual strain gauge was used in the DIC to mimic the strain gauge data. Since the quality of the DIC measurement is dependent on the signal-to-noise ratio, an optimal DIC settings [42] are desirable to accurately measure the strains at low loads. While the optimal DIC settings are usually determined by performance analysis [43], the representative value of the Poisson's ratio for the selected DIC settings is determined here by a simple engineering method.

The results of both experimental parts are presented in Section 3.

1 VIRTUAL EXPERIMENTATION

In this section a methodology of virtual experimentation using DIC is presented. The concept has been first introduced by Lava et al. [44]. The idea is to perform a FEM simulation of experiment with known outcome, followed by synthetic deformation of synthetically generated random speckle pattern to obtain deformed images for DIC processing. Finally, the deformed images are processed by DIC to obtain displacement and strain fields, which can be easily compared with original FEM result. The methodology is employed for a comparison of Poisson's ratio obtained with virtual strain gauge technique and virtual full field DIC measurements.

1.1 FEM Model

The most common test for determination of Poisson's ratio of rock is uniaxial compression test of cylindrical sample [45], which is in case of virtual experimentation replicated by FEM simulation in ABAQUS computational software [46]. Based on similar studies, literature and FEM modelling approaches [47] to [50], a numerical model of cylindrical rock-like specimen was created with diameter of 50 mm and height of 100 mm. To capture heterogeneous structure on the mesoscale, two-phase material model is used: a softer matrix with harder rock grain spherical inclusion. Both phases are considered as a linear elastic with material properties given in Table 1.

Table 1. *Material properties*

Phase	Elastic modulus [GPa]	Poisson's ratio [/]
Matrix	70	0.1
Inclusions (rock grains)	140	0.2

For the hard inclusion phase, a model with randomly distributed spherical inclusions with a variable diameter of 0.5 mm to 2 mm is used. It is important to note that despite the assumption

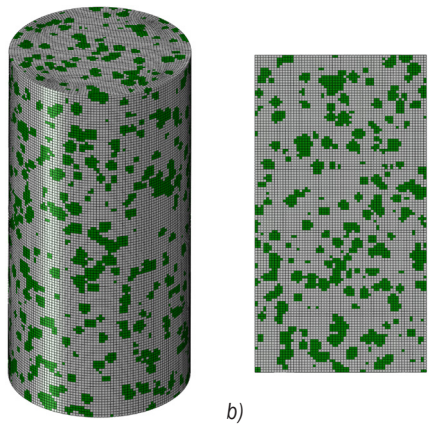

a) b)

Fig. 1. *a) Domain discretization with inclusions in green, and b) its diametral plane cross-section*

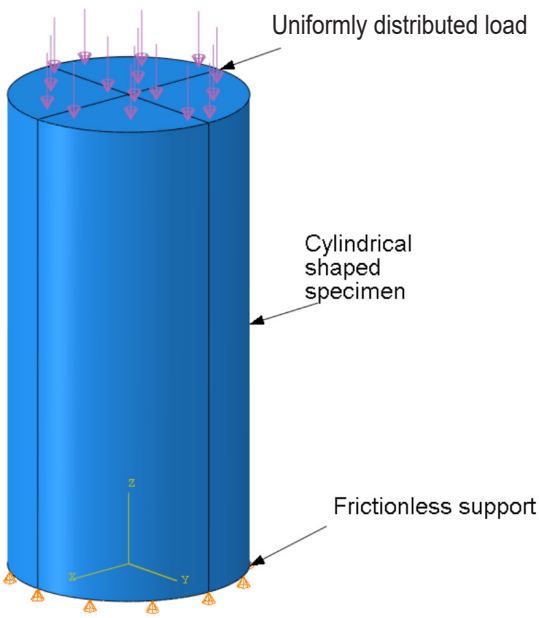

Fig. 2. *Numerical model of cylindrical specimen*

of spherical inclusions in the model, the resulting inclusion phase is not necessarily spherical due to the coalescence of inclusions. The volume ratio of the inclusion phase to the total volume of the specimen is 23 %. To integrate the inclusion phase into the numerical model, a dense mesh of small cubes was initially created. For each cube the material properties of the matrix or inclusion is assigned, depending on its position. For this purpose, mathematical model is developed using the Python scripting language to simulate a space populated by randomly distributed spheres, each varying in size. If the element centroidal coordinate is located inside a sphere, the inclusion modulus of elasticity and Poisson's ratio is assigned to the element. Otherwise, the material properties of the element are belonging to the matrix phase. The global seed size of the mesh was set to 0.8 mm and linear hexahedral elements (ABAQUS designation C3D8R) with reduced integration were used. Fig. 1 shows the mesh of the numerical model, with the matrix elements in grey and the hard rock inclusion elements in green.

The model is supported on the bottom surface in axial direction, whereas the radial and circumferential displacements are not restrained. On the top surface, uniformly distributed force of magnitude 30 kN is compressing the cylinder. Loading conditions are shown on Fig. 2.

1.2 Determination of Poisson's Ratio

Only surface strains from the simulation results that could also be measured in the actual experiment are used to calculate the Poisson's ratio. The strains used for the calculation are extracted in two ways: firstly, to mimic the conventional strain gauge measurements and secondly, to mimic the DIC full-field measurements. With both methods, the Poisson's ratio is calculated for a population of randomly positioned strain gauges and ROIs from DIC results. Finally, the Poisson's ratios obtained for both methods are compared.

1.2.1 Strain Gauge Imitation

Two rectangles, representing strain gauges, are placed next to each other and randomly on the surface of the specimen. The rectangles are 20 mm long and 10 mm wide. One rectangle is oriented vertically to determine the axial strain and the other horizontally to determine the circumferential strain.

The axial or circumferential strains are extracted from the model as the averaged strains of the finite elements within the rectangle. This value is then assigned to the individual strain gauge measurement. This is repeated for both vertically and horizontally oriented rectangles, resulting in an average axial strain $\varepsilon_{\parallel,i}$ and circumferential strain $\varepsilon_{\perp,i}$. The index i represents an individual position of a pair of rectangles, as shown in Fig. 3.

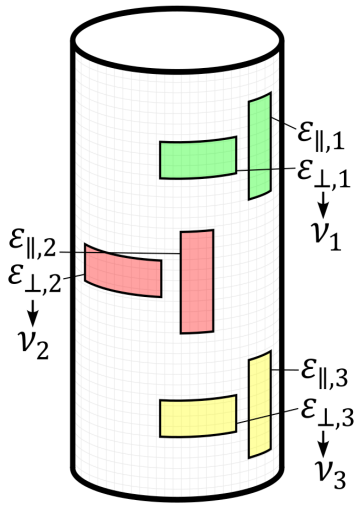

Fig. 3. *Poisson's ratio determination from multiple randomly positioned quasi strain gauges*

Poisson's ratio for i^{th} location is then calculated as

$$\nu_i = -\frac{\varepsilon_{\perp,i}}{\varepsilon_{\parallel,i}}, \tag{1}$$

and the calculation procedure repeated n-times, which finally represents the population of Poisson's ratios ν_i, $i \in \{1,2,...,n\}$. From these results we can observe scattering of locally determined Poisson's ratios on inhomogeneous strain field.

1.2.2 DIC Virtual Experimentation

The aim of the virtual DIC experiments is to analyse how the measured strain fields are influenced by systematic and random errors that propagate throughout the entire DIC measurement chain. For this purpose, the measurement itself must be compared with the "ground truth" result, which can be obtained from a finitelement simulation, for example. Essentially, such a methodology can be used to analyse not only the influence of the material structure itself, but also the influence of the DIC system settings on the final result. For this purpose, a concept of virtual DIC experimentation is presented in Fig. 4.

In the first step (Fig. 4a), a FEM simulation with 60 monotonically increasing load increments up to the axial force 30 kN is carried out in accordance with Section 1.1. From the simulation, the displacements of the specimen's surface and the corresponding reference strain fields are calculated. The displacement field is then used in the MatchID software to generate a synthetically deformed images (Fig. 4b) of a reference speckle pattern (Bossuyt et al. [51]). These images serve as a surrogate for the actual images normally captured by charge-coupled device (CCD) or complementary metal–oxide–semiconductor (CMOS) cameras. In this case, however, the deformation of the images is known, as it was imposed by the reference simulation. In the final step, the deformed images are processed with the DIC algorithm to reconstruct the reference displacement and the strain field under the applied DIC settings (Fig. 4c). Assuming that the image deformation algorithm does not introduce significant errors into the FEM displacements, the difference between the reconstructed DIC and FEM displacement and strain field results solely from the digitalisation process and the DIC algorithm.

Poisson's ratios are finally calculated for randomly positioned regions of interest over a complete circumference of the specimen, typically covering approximately 80 % of the total height of the cylinder and 80° of its circumferences to mimic the ROI normally captured with a stereo DIC.

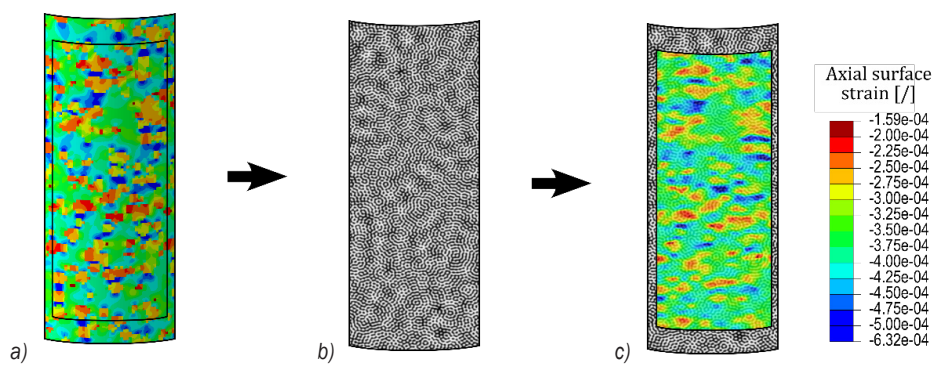

Fig. 4. *DIC virtual experimentation procedure: a) FEM simulation with a well-characterized material, b) deformed images based on the calculated displacement field and a random speckle pattern, and c) reconstruction of strain fields from the deformed images using the DIC algorithm*

2 EXPERIMENTAL TEST

For validation, the uniaxial compression test is performed experimentally, whereby the Poisson's coefficient is measured by (i) the quasi-strain gauge technique, and (ii) with DIC. The reason for using quasi strain gauges instead of true strain gauges is that gluing dozens of strain gauges is impractical and unfeasible because the adhesive would eventually impair the surface of the sample. For this reason, a similar method to that described in Section 1.2.1 was used, but instead of the strains from the FEM simulation, the strains from the DIC were used. Of course, such an approach only mimics an averaging effect of the strain gauge measurement and completely neglects the uncertainties caused by the physical measurement chain.

However, based on the retrieved data on strains either with quasi strain gauge or DIC, the Poisson's ratio from the quasi strain gauge and the DIC strain field measurements is finally calculated and compared.

2.1 Experimental Setup

A cylindrical specimen with a diameter of 42 mm and a height of 82 mm is used for the uniaxial compression test. The samples consist of sandstone material with visible inclusions on the surface of the sample (Fig. 5) and is manufactured according to the ASTM-D4543 [52] requirements. The samples are machined to produce smooth surfaces and parallel contact surfaces in order to create homogeneous loading conditions on the macro level.

Fig. 5. *Sandstone cylindrical specimen with visible inclusions on the surface*

The specimen is placed on flat steel platens in a custom-made universal testing machine (load capacity 50 kN with 50 kN Class 1 force transducer for the measurement of static or dynamic loads in tension or compression) and tested according to the ASTM D7012 [53]. The strain fields are measured using stereo DIC equipment, with the cameras mounted at an angle of approximately 30°, as shown in Fig. 6.

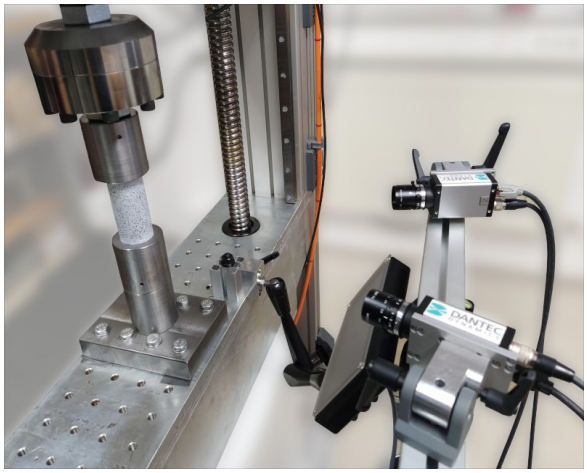

Fig. 6. *Uniaxial compression test setup with stereo DIC measurement system*

The black coloured random speckle pattern is applied on the white painted cylindrical surface as shown on Fig. 7. The strain resolution has been measured by taking a pair of still images which were postprocessed by DIC algorithm [54]. Here, a strain resolution of $\varepsilon = 2.6 \times 10^{-4}$ was found for both circumferential and axial direction. The adopted DIC equipment and settings are specified in Table 1 [55] while at the same time avoiding strain concentrations near sample edges where Digital Image Correlation (DIC.

Fig. 7. *Random black speckle pattern on the white background colour applied to the surface of the actual specimen*

Table 1. *DIC and setup settings used to process the deformed images and determine the strain fields*

Technique and DIC software	2D DIC, Dantec Dynamics, Istra 4D
Cameras	Manta G-201B, Allied Vision, 2 pieces
Image resolution	2464 px × 1228 px
Objective focal distance	300 mm (approximate)
Field of view	64 mm × 26 mm
Stereo angle	26.5° (approximate)
Illumination colour temp.	4400 K
Pattering technique	white composite surface with black speckles
Pattern feature size	13 px
DIC technique	stereo
Subset size	61px
Step size	31px
Subset weight	uniform
Subset shape function	affine
Matching criterion	Approximated sum of squared differences
Interpolant	Local bicubic spline interpolation
Strain calculation method	Direct from the subset shape function
Reference image	Fixed
Data points	860
Temporal smoothing	none
Acquisition frequency	3.3 Hz
Specimen length	82 mm
Specimen width	42 mm
Loading speed	0.02 mm/s

The specimen was loaded 80 times at a displacement rate of 0.02 mm/s until the maximum force of 33 kN was reached. For each measurement, different portion of the specimen was recorded and postprocessed by the DIC algorithm to obtain the strain fields. The cameras were repositioned and recalibrated between the tests.

2.2 Postprocessing

To validate the results of the virtual experiments from Section 1, quasi strain gauge data is extracted from the measured strain fields, which is done in a similar way to Section 1.2.1. The mean value of the axial and circumferential strain is extracted from vertically and horizontally arranged rectangular areas. The rectangles represent strain gauges that are 20 mm long and 10 mm wide. A pair of rectangles is placed side by side approximately in the centre of the region of interest. The Poisson's ratio is calculated based on the extracted strains of the quasi-strain gauges. The procedure is repeated for each measurement to obtain a distribution of the calculated Poisson's ratios, extracted at the maximum load.

When using DIC, the ROI is constrained to the centre of the sample within the field of view as presented in Fig. 8. To avoid edge effects, the ROI occupies about 80 % of the height of the sample, similar to the virtual experiment. The Poisson's ratio is calculated individually for each strain measurement and the calculated values are then averaged to obtain a single value for the Poisson's ratio for one measurement. Typical strain measurement is presented in Fig. 8. Finally, the procedure is repeated for each measurement.

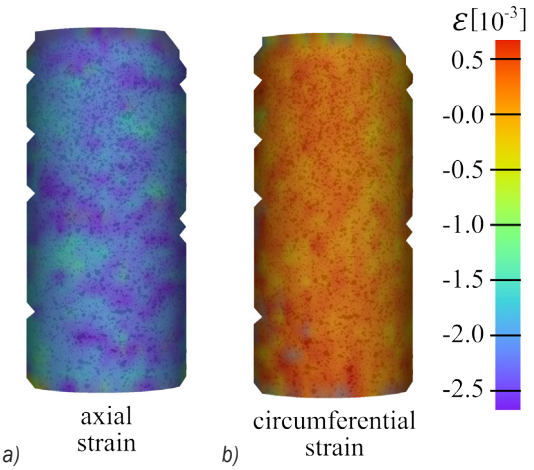

Fig. 8. *a) Axial, and b) circumferential strain field measured by DIC*

3 RESULTS

In this section the distributions of calculated Poisson's ratio are presented for virtual and experiments for quasi strain gauge and DIC processed data.

3.1 The Results of Virtual Testing

As described in Section 1, the data from the randomly placed quasi strain gauges are extracted from the FEM simulation results and used to calculate the Poisson's ratios. Similarly, the DIC data is reconstructed from the FEM simulation results using the concept of virtual experiments. For both quasi-strain gauges and DIC, 1000 repetitions of the measurement were independently analysed for the probability distribution of the Poisson's coefficient. The mean value of the coefficient when using strain gauges and DIC is 0.131 for both cases, while the standard deviation when using strain gauges is about 3.4 times larger (0.00588 for the strain gauge measurement compared to 0.00173 for DIC). The probability distributions for both measurement methods are shown in the histogram in Fig. 9, where the green bars correspond

to the population determined with quasi-strain gauges and the red bars to the measurement with DIC. The statistical data of the populations are shown in tabular form as insets.

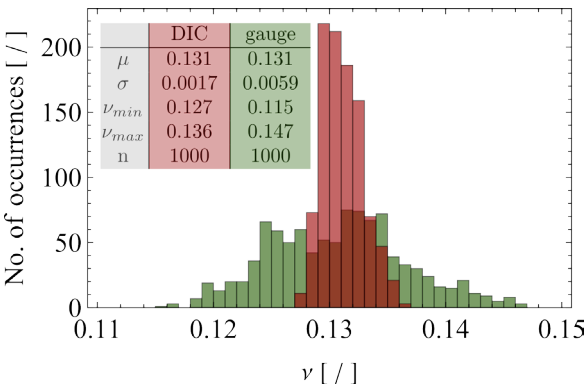

Fig. 9. *Distribution of Poisson's ratios determined by virtual strain gauge (green) and full-field DIC data (red)*

3.2 Experimental Test Results

The same analysis was performed for the actual experimental data. In this particular case, a total of 80 repetitions of the actual experiment were performed for both quasi strain gauges and DIC. The probability distributions for both measurement methods are shown in Fig. 10, with the green bars corresponding to the strain gauge measurements and the red bars to the DIC measurements.

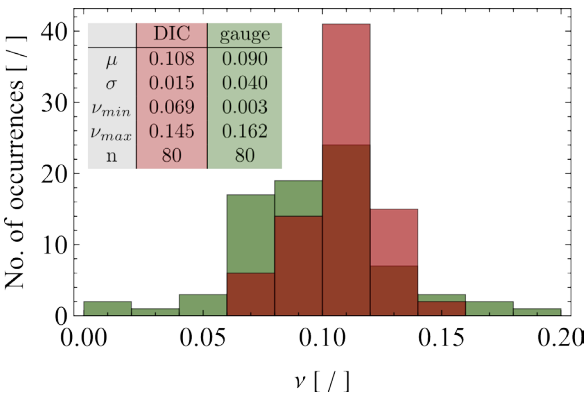

Fig. 10. *Distribution of Poisson's ratio determined by virtual strain gauge data (green) and full-field DIC measurements (red)*

The measured mean value of the Poisson's coefficients for the quasi strain gauge technique is 0.0896, while the value for DIC is slightly higher (0.108). When analysing the standard deviation of the two measured populations, a consistent result with the virtual experiment is obtained. In the particular case, the standard deviation for quasi strain gauge data is 0.0404, while this value for DIC is 0.0152, which is approximately 2.7 times smaller.

3.3 RVE Value for Poisson's Ratio

Despite the superiority of DIC measurements over conventional strain gauge measurement technology, the reliability of DIC measurements in terms of spatial resolution, accuracy, precision, and sensitivity as well as data accuracy is still debated today. For example, it is known that there is a trade-off between spatial resolution and precision, which is determined and influenced by the DIC settings [56]. Furthermore, determining the spatial resolution of a measurement is not as straightforward and often requires à priori tests with the same test conditions as the actual tests or the specification of a synthetic displacement field with known variations in the displacement field [57].

In this particular case, the measurement of small strain fields with strain gauges or DIC is a challenge due to the signal-to-noise ratio in the strain fields [58]. For this purpose, an alternative criterion is proposed to determine the accurate value of Poisson's ratio with DIC under the assumption that the material behaviour is isotropic at the macro level.

When analysing the complete strain fields in the sample, DIC has a considerable advantage over strain gauges. In particular, not only can a complete strain field be measured, as shown in Fig. 8, but these strains can also be analysed in different coordinate systems, as shown in Fig. 11.

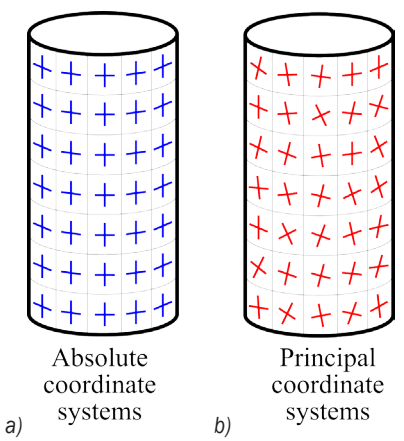

Fig. 11. *Schematic representation of the alignment of absolute, and principal coordinate systems*

As demonstrated in the figure, the strain field can be observed in the absolute (Cartesian) coordinate system, with axes aligned in axial and circumferential directions or in the principal strains coordinate system.

In the latter case, if the observed strains are dominated by noise, the principal directions in different material points on specimen's surface are not aligned, they are randomly oriented, instead. In the undesired case of non-alignment of platens and specimen's contact surfaces the principal strain axes also differ from absolute coordinate system axes. However, in that case the principal coordinate system follows some regular pattern on the specimen's surface (strain trajectories).

Typical axial and circumferential strain evolution of individual subset in absolute coordinate system is presented in Figs. 12 and 13, respectively.

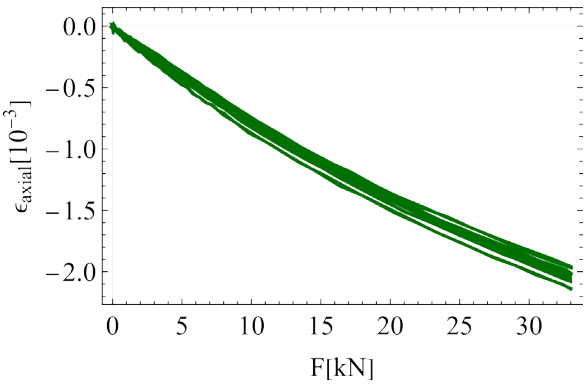

Fig. 12. *Evolution of axial strain in relation to the magnitude of applied load in absolute coordinate system*

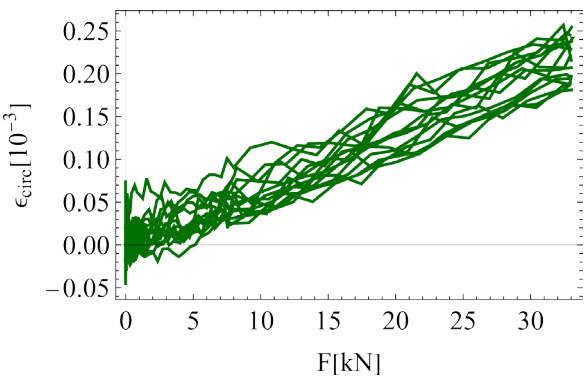

Fig. 13. *Evolution of circumferential strain in relation to the magnitude of applied load in absolute coordinate system*

In Fig. 14, the mean value of the Poisson's ratio calculated from these measured strain fields is displayed with blue curves. As shown, high variations of the Poisson's ratio gradually diminish as the loading force increases. The higher the load, the higher the signal, while the noise floor level remains roughly constant for DIC. Red curves represent the mean Poisson's ratio, defined as a ratio of minor versus major strain, i.e., the ratio is calculated in principal strains coordinate system. Similar to the absolute coordinate system, due to the low signal-to-noise ratio a high variation of Poisson's ratio at the beginning of loading can be seen. The degree of alignment between absolute and principal coordinate systems can be measured by calculating the relative difference in the mean values of the Poisson's ratio. In order to ensure a satisfactory level of alignment, a threshold of 5 % is employed.

For the particular case from Fig. 14, this occurs at force of 15 kN. This value represents the smallest force required to reliably measure the representative value of the Poisson's ratio for the given specimen size and material composition.

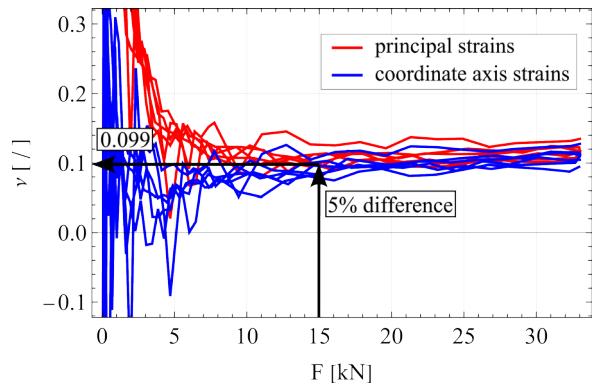

Fig. 14. *Poisson's ratio versus loading rate*

4 DISCUSSION AND CONCLUSIONS

While the strain gauge measuring technique has not evolve in the recent decades, DIC has flourished with the development of computational technology. The equipment has nowadays become publicly and commercially accessible and user-friendly.

The results presented in Section 3.1 and Section 3.2 show that the Poisson's ratio can be measured with DIC with a smaller margin of error than with the conventional strain gauge technique. Smaller margin of error can be generally achieved in DIC by improving strain resolution via increasing subset size or image resolution. In the synthetic experiment, the difference between the standard deviation of the population of measured values is 3.4 times larger in favour of DIC, while this value is 2.7 in the actual experiment. The main reason for this is that DIC provides a larger population of values since the measurement is performed for a complete region of interest each time and the richness of the measured field can be utilised for the particular case when the representative value is determined from the mean. On the other hand, when using conventional strain gauges, there is always the possibility that a local response of the substructure to

which the gauge is attached is measured. To avoid this problem and possibly eliminate this systematic error, it is advisable to repeat the experiment several times. To substantiate this claim, consider the simulated and measured strain field in Fig. 4. As shown, the inclusion phase locally influences the axial strain field, which can be accurately reproduced by the DIC (note that the legend for the FEM simulation and the DIC results is the same and the strain field distribution is obviously very similar). This example demonstrates (i) the importance of virtual DIC testing for experiment design and (ii) the ability of DIC to measure and exploit the richness of resulting strain fields. In addition, for most samples with only few test opportunities available, the full-field methods are advantageous over the conventional strain gauge method. If the experiment is carried out to failure, the captured images can be processed repeatedly using DIC with different settings, which can be optimised by performance analysis **[37]**.

Finally, it should be noted that the measurement of the Poisson ratio is constrained by the signal-to-noise ratio. When observing the mean and standard deviation of the ratio, a larger standard deviation can be observed at lower load magnitudes. However, this value decreases as the load increases. At this stage, DIC proves to be advantageous compared to strain gauges because the strain fields can be observed in multiple coordinates systems simultaneously, for example in the principal and absolute coordinate systems. If the Poisson's ratio is also defined in the principal coordinate system, the comparison of the coefficient immediately indicates whether the coordinate systems are not aligned or not. The relative discrepancy between the mean values measured in both coordinate systems can be used to determine an engineering criterion for the smallest load value required to reliably measure the representative value of the coefficient.

5 ACKNOWLEDGEMENT

The author would like to thank the staff of the Laboratory for Numerical Modelling and Simulation at the University of Ljubljana, Faculty of Mechanical Engineering, for the use of laboratory equipment and for generously providing access to the MatchID software, which was crucial for the realization of this research.

6 REFERENCES

[1] Jaeger, J.C., Cook, N.G.W., Zimmerman, R. (2009). *Fundamentals of Rock Mechanics*, John Wiley & Sons, Hoboken.

[2] Zhou, T., Chen, J., Xie, H., Zhou, C., Wang, F., Zhu, J. (2022). Failure and mechanical behaviors of sandstone containing a pre-existing flaw under compressive-shear loads: Insight from a digital image correlation (DIC) analysis. *Rock Mechanics and Rock Engineering*, vol. 55, no. 7, p. 4237-4256, **DOI:10.1007/s00603-022-02861-4**.

[3] Bernabé, Y., Fryer, D.T., Shively, R.M. (1994). Experimental observations of the elastic and inelastic behaviour of porous sandstones. *Geophysical Journal International*, vol. 117, no. 2, p. 403-418, **DOI:10.1111/j.1365-246X.1994.tb03940.x**.

[4] Schultz, R.A. (1996). Relative scale and the strength and deformability of rock masses. *Journal of Structural Geology*, vol. 18, no. 9, p. 1139-1149, **DOI:10.1016/0191-8141(96)00045-4**.

[5] Sari, M. (2021). Determination of representative elementary volume (REV) for jointed rock masses exhibiting scale-dependent behavior: a numerical investigation. *International Journal of Geo-Engineering*, vol. 12, no. 1, p. 34, **DOI:10.1186/s40703-021-00164-1**.

[6] Wang, X., Zhao, Y., Lin, X. (2011). Determination of mechanical parameters for jointed rock masses. *Journal of Rock Mechanics and Geotechnical Engineering*, vol. 3, p. 398-406, **DOI:10.3724/SP.J.1235.2011.00398**.

[7] Wu, Q., Kulatilake, P.H.S.W. (2012). REV and its properties on fracture system and mechanical properties, and an orthotropic constitutive model for a jointed rock mass in a dam site in China. *Computers and Geotechnics*, vol. 43, p. 124-142, **DOI:10.1016/j.compgeo.2012.02.010**.

[8] Cao, Y.J., Shen, W.Q., Shao, J.F., Wang, W. (2021). A multi-scale model of plasticity and damage for rock-like materials with pores and inclusions. *International Journal of Rock Mechanics and Mining Sciences*, vol. 138, 104579, **DOI:10.1016/j.ijrmms.2020.104579**.

[9] Yu, Z., Shao, J.-F., Vu, M.-N., Armand, G. (2021). Numerical study of thermo-hydro-mechanical responses of in situ heating test with phase-field model. *International Journal of Rock Mechanics and Mining Sciences*, vol. 138, 104542, **DOI:10.1016/j.ijrmms.2020.104542**.

[10] Potyondy, D.O., Cundall, P.A. (2004). A bonded-particle model for rock. *International Journal of Rock Mechanics and Mining Sciences*, vol. 41, no. 8, p. 1329-1364, **DOI:10.1016/j.ijrmms.2004.09.011**.

[11] Zhou, C., Xie, H., Zhu, J. (2024). Revealing Size effect and associated variability of rocks based on BPM-μDFN modelling: Significance of internal microstructure and strain rate. *Rock Mechanics and Rock Engineering*, **DOI:10.1007/s00603-023-03653-0**.

[12] Zhou, C., Xie, H., Wang, Z., Zhou, T., Zhu, J. (2023). A novel fractal-statistical scaling model of rocks considering strain rate. *Journal of Rock Mechanics and Geotechnical Engineering*, vol. 15, no. 11, p. 2831-2841, **DOI:10.1016/j.jrmge.2023.02.033**.

[13] Zhou, C., Xu, C., Karakus, M., Shen, J. (2018). A systematic approach to the calibration of micro-parameters for the flat-jointed bonded particle model. *Geomechanics and Engineering*, vol. 16, no. 5, p. 471-482.

[14] Vrh, M., Halilovič, M., Starman, B., Štok, B. (2011). A new anisotropic elasto-plastic model with degradation of elastic modulus for accurate springback simulations. *International Journal of Material Forming*, vol. 4, no. 2, p. 217-225, **DOI:10.1007/s12289-011-1029-8**.

[15] Starman, B., Vrh, M., Halilovič, M., Štok, B. (2014). Advanced modelling of sheet metal forming considering anisotropy and Young's modulus evolution. *Strojniški vestnik - Journal of Mechanical Engineering*, vol. 60, no. 2, p. 84-92, **DOI:10.5545/sv-jme.2013.1349**.

[16] Halilovič, M., Starman, B., Coppieters, S. (2024). Computationally efficient stress reconstruction from full-field strain measurements. *Computational Mechanics*, **DOI:10.1007/s00466-024-02458-4**.

[17] Schreier, H., Orteu, J.-J., Sutton, M.A. (2009). *Image Correlation for Shape, Motion and Deformation Measurements: Basic Concepts, Theory and Applications*, Springer, Boston, **DOI:10.1007/978-0-387-78747-3**.

[18] Pierron, F. (2023). Material testing 2.0: A brief review. *Strain*, vol. 59, no. 3, e12434, **DOI:10.1111/str.12434**.

[19] Maček, A., Urevc, J., Halilovič, M. (2021). Flat specimen shape recognition based on full-field optical measurements and registration using mapping error minimization method. *Strojniški vestnik - Journal of Mechanical Engineering*, vol. 67, no, 5, p. 203-213, **DOI:10.5545/sv-jme.2021.7111**.

[20] Maček, A., Starman, B., Mole, N., Halilovič, M. (2020). Calibration of advanced yield criteria using uniaxial and heterogeneous tensile test data. *Metals*, vol. 10, no. 4, 542, **DOI:10.3390/met10040542**.

[21] Obid, Š., Halilovič, M., Urevc, J., Starman, B. (2023). Non-linear elastic tension-compression asymmetric anisotropic model for fibre-reinforced composite materials. *International Journal of Engineering Science*, vol. 185, 103829, **DOI:10.1016/j.ijengsci.2023.103829**.

[22] Verbruggen, S., De Sutter, S., Iliopoulos, S., Aggelis, D.G., Tysmans, T. (2015). Experimental structural analysis of hybrid composite-concrete beams by digital image correlation (DIC) and acoustic emission (AE). *Journal of Nondestructive Evaluation*, vol. 35, no. 1, 2, **DOI:10.1007/s10921-015-0321-9**.

[23] Maček, A., Urevc, J., Žagar, T., Halilovič, M. (2021). Crimp joint with low sensitivity to process parameters: numerical and experimental study. *International Journal of Material Forming*, vol. 14, no. 5, p. 1233-1241, **DOI:10.1007/s12289-021-01637-5**.

[24] Tang, Y., Zhang, H., Guo, X., Ren, T. (2022). Literature survey and application of a full-field 3D-DIC technique to determine the damage characteristic of rock under triaxial compression. *International Journal of Damage Mechanics*, vol. 31, no. 7, p. 1082-1095, **DOI:10.1177/10567895221089660**.

[25] Marek, A., Davis, F.M., Pierron, F. (2017). Sensitivity-based virtual fields for the non-linear virtual fields method, *Computational Mechanics*, vol. 60, no. 3, p. 409-431, **DOI:10.1007/s00466-017-1411-6**.

[26] Zhang, Y., Yamanaka, A., Cooreman, S., Kuwabara, T., Coppieters, S. (2023). Inverse identification of plastic anisotropy through multiple non-conventional mechanical experiments. *International Journal of Solids and Structures*, vol. 285, 112534, **DOI:10.1016/j.ijsolstr.2023.112534**.

[27] Yin, Y., Liu, G., Zhao, T., Ma, Q., Wang, L., Zhang, Y. (2022). Inversion method of the young's modulus field and Poisson's ratio field for rock and its test application. *Materials*, vol. 15, no. 15, 5463, **DOI:10.3390/ma15155463**.

[28] Satošek, R., Pepelnjak, T., Starman, B. (2023). Characterisation of out-of-plane shear behaviour of anisotropic sheet materials based on indentation plastometry. *International Journal of Mechanical Sciences*, vol. 253, 108403, **DOI:10.1016/j.ijmecsci.2023.108403**.

[29] Starman, B., Vrh, M., Koc, P., Halilovič, M. (2019). Shear test-based identification of hardening behaviour of stainless steel sheet after onset of necking. *Journal of Materials Processing Technology*, vol. 270, p. 335-344, **DOI:10.1016/j.jmatprotec.2019.03.010**.

[30] Zhang, K., Zhang, K., Liu, W., Xie, J. (2023). A novel DIC-based methodology for crack identification in a jointed rock mass. *Materials & Design*, vol. 230, 111944, **DOI:10.1016/j.matdes.2023.111944**.

[31] Chai, J., Liu, Y., OuYang, Y., Zhang, D., Du, W. (2020). Application of digital image correlation technique for the damage characteristic of rock-like specimens under uniaxial compression. *Advances in Civil Engineering*, vol. 2020, e8857495, **DOI:10.1155/2020/8857495**.

[32] Chen, J., Yin, X., Zhou, C., Pan, M., Han, Z., Zhou, T. (2023). Interaction between flaws and failure characteristics of red sandstone containing double flaws under compressive-shear loading. *Engineering Fracture Mechanics*, vol. 292, 109664, **DOI:10.1016/j.engfracmech.2023.109664**.

[33] Luo, P., Li, D., Ma, J., Zhou, A., Zhang, C. (2023). Experimental investigation on mechanical properties and deformation mechanism of soft-hard interbedded rock-like material based on digital image correlation. *Journal of Materials Research and Technology*, vol. 24, p. 1922-1938, **DOI:10.1016/j.jmrt.2023.03.145**.

[34] Wang, F., Xie, H., Zhou, C., Wang, Z., Li, C. (2023). Combined effects of fault geometry and roadway cross-section shape on the collapse behaviors of twin roadways: An experimental investigation. *Tunnelling and Underground Space Technology*, vol. 137, 105106, **DOI:10.1016/j.tust.2023.105106**.

[35] Xing, H.Z., Zhang, Q.B., Ruan, D., Dehkhoda, S., Lu, G.X., Zhao, J. (2018). Full-field measurement and fracture characterisations of rocks under dynamic loads using high-speed three-dimensional digital image correlation. *International Journal of Impact Engineering*, vol. 113, p. 61-72, **DOI:10.1016/j.ijimpeng.2017.11.011**.

[36] Zhang, Q.B., Zhao, J. (2013). Determination of mechanical properties and full-field strain measurements of rock material under dynamic loads. *International Journal of Rock Mechanics and Mining Sciences*, vol. 60, p. 423-439, **DOI:10.1016/j.ijrmms.2013.01.005**.

[37] Hsieh, A., Dyskin, A.V., Dight, P. (2014). The increase in Young's modulus of rocks under uniaxial compression. *International*

Journal of Rock Mechanics and Mining Sciences, vol. 70, p. 425-434, **DOI:10.1016/j.ijrmms.2014.05.009**.

[38] Liu, Z., Wang, H., Yuan, L., Zhang, B., Wang, W., Ma, Z., Xue, Y., Li, Y. (2020). A new test method and system for the circumferential deformation of cylindrical standard specimens in geotechnical mechanics and its application. *Measurement*, vol. 149, 107041, **DOI:10.1016/j.measurement.2019.107041**.

[39] Isah, B.W., Mohamad, H., Ahmad, N.R., Harahap, I.S.H., Al-Bared, M.A.M. (2020). Uniaxial compression test of rocks: Review of strain measuring instruments. *IOP Conference Series: Earth and Environmental Science*, vol. 476, no. 1, 012039, **DOI:10.1088/1755-1315/476/1/012039**.

[40] Sun, C., Tang, G., Chapman, S., Zhang, H., Fortin, J., Wang, S., Pan, D., Yue, J. (2023). A numerical assessment of local strain measurements on the attenuation and modulus dispersion in rocks with fluid heterogeneities. *Geophysical Journal International*, vol. 235, no. 1, p. 951-969, **DOI:10.1093/gji/ggad289**.

[41] Maček, A., Starman, B., Coppieters, S., Urevc, J., Halilovič, M. (2024). Confidence intervals of inversely identified material model parameters: A novel two-stage error propagation model based on stereo DIC system uncertainty. *Optics and Lasers in Engineering*, vol. 174, 107958, **DOI:10.1016/j.optlaseng.2023.107958**.

[42] Yang, D., Bornert, M., Gharbi, H., Valli, P., Wang, L.L. (2010). Optimized optical setup for DIC in rock mechanics. *EPJ Web of Conferences*, vol. 6, 22019, **DOI:10.1051/epjconf/20100622019**.

[43] Gothivarekar, S., Coppieters, S., Van de Velde, A., Debruyne, D. (2020). Advanced FE model validation of cold-forming process using DIC: Air bending of high strength steel. *International Journal of Material Forming*, vol. 13, no. 3, p. 409-421, **DOI:10.1007/s12289-020-01536-1**.

[44] Lava, P., Cooreman, S., Coppieters, S., De Strycker, M., Debruyne, D. (2009). Assessment of measuring errors in DIC using deformation fields generated by plastic FEA. *Optics and Lasers in Engineering*, vol. 47, no. 7, p. 747-753, **DOI:10.1016/j.optlaseng.2009.03.007**.

[45] Xue, L., Qin, S., Sun, Q., Wang, Y., Lee, L. M., Li, W. (2014). A study on crack damage stress thresholds of different rock types based on uniaxial compression tests. *Rock Mechanics and Rock Engineering*, vol. 47, no. 4, p. 1183-1195, **DOI:10.1007/s00603-013-0479-3**.

[46] ABAQUS User's Manual (2012). *Fortran, Python*, SIMULIA, Providence.

[47] Li, M., Guo, P., Stolle, D., Liang, L. (2017). Modeling method for a rock matrix with inclusions distributed and hydraulic fracturing characteristics. *Journal of Petroleum Science and Engineering*, vol. 157, p. 409-421, **DOI:10.1016/j.petrol.2017.07.017**.

[48] Wu, Z., Wong, L.N.Y. (2013). Modeling cracking behavior of rock mass containing inclusions using the enriched numerical manifold method. *Engineering Geology*, vol. 162, p. 1-13, **DOI:10.1016/j.enggeo.2013.05.001**.

[49] Ren, M., Zhao, G., Zhou, Y. (2022). Elastic stress transfer model and homogenized constitutive equation for the multi-phase geomaterials. *Engineering Geology*, vol. 306, 106631, **DOI:10.1016/j.enggeo.2022.106631**.

[50] Tang, C.A., Fu, Y.F., Kou, S.Q., Lindqvist, P.-A. (1998). Numerical simulation of loading inhomogeneous rocks. *International Journal of Rock Mechanics and Mining Sciences*, vol. 35, no. 7, p. 1001-1007, **DOI:10.1016/S0148-9062(98)00014-X**.

[51] Bossuyt, S. (2013). Optimized patterns for digital image correlation, Jin, H. Sciammarella, C. Furlong, C., Yoshida, S. (eds.). *Imaging Methods for Novel Materials and Challenging Applications*, Volume 3, Springer, New York, p. 239-248, **DOI:10.1007/978-1-4614-4235-6_34**.

[52] ASTM (2019). *Standard Practices for Preparing Rock Core as Cylindrical Test Specimens and Verifying Conformance to Dimensional and Shape Tolerances*, ASTM International, West Conshohocken, **DOI:10.1520/D4543-19**.

[53] ASTM (2014). *Standard Test Methods for Compressive Strength and Elastic Moduli of Intact Rock Core Specimens under Varying States of Stress and Temperatures*, ASTM International, West Conshohocken, **DOI:10.1520/D7012-14E01**.

[54] Zhang, Y., Gothivarekar, S., Conde, M., de Velde, A.V., Paermentier, B., Andrade-Campos, A., Coppieters, S. (2022). Enhancing the information-richness of sheet metal specimens for inverse identification of plastic anisotropy through strain fields. *International Journal of Mechanical Sciences*, vol. 214, 106891, **DOI:10.1016/j.ijmecsci.2021.106891**.

[55] Jones, E.M.C., Corona, E., Jones, A. R., Scherzinger, W.M., Kramer, S.L.B. (2021). Anisotropic plasticity model forms for extruded Al 7079: Part II, validation. *International Journal of Solids and Structures*, vol. 213, p. 148-166, **DOI:10.1016/j.ijsolstr.2020.11.031**.

[56] Fazzini, M., Mistou, S., Dalverny, O., Robert, L. (2010). Study of image characteristics on digital image correlation error assessment. *Optics and Lasers in Engineering*, vol. 48, no. 3, p. 335-339, **DOI:10.1016/j.optlaseng.2009.10.012**.

[57] Forsström, A., Bossuyt, S., Scotti, G., Hänninen, H. (2020). Quantifying the effectiveness of patterning, test conditions, and DIC parameters for characterization of plastic strain localization. *Experimental Mechanics*, vol. 60, no. 1, p. 3-12, **DOI:10.1007/s11340-019-00510-6**.

[58] Acciaioli, A., Lionello, G., Baleani, M. (2018). Experimentally achievable accuracy using a digital image correlation technique in measuring small-magnitude (<0.1%) homogeneous strain fields. *Materials*, vol. 11, no. 5, 751, **DOI:10.3390/ma11050751**.